condensed matter

MDPI

Article

On the Nanoscale Structure of $K_xFe_{2-y}Ch_2$ (*Ch* = S, Se): A Neutron Pair Distribution Function View

Panagiotis Mangelis [1,*], Hechang Lei [2,†], Marshall T. McDonnell [3], Mikhail Feygenson [3,‡], Cedomir Petrovic [2], Emil S. Bozin [2] and Alexandros Lappas [1]

1 Institute of Electronic Structure and Laser, Foundation for Research and Technology—Hellas, Vassilika Vouton, 711 10 Heraklion, Greece; lappas@iesl.forth.gr
2 Condensed Matter Physics and Materials Science Department, Brookhaven National Laboratory, Upton, NY 11973, USA; hlei@ruc.edu.cn (H.L.); petrovic@bnl.gov (C.P.); bozin@bnl.gov (E.S.B.)
3 Neutron Scattering Division, Oak Ridge National Laboratory, Oak Ridge, TN 37831, USA; mcdonnellmt@ornl.gov (M.T.M.); m.feygenson@fz-juelich.de (M.F.)
* Correspondence: mangelis@iesl.forth.gr
† Present Address: Department of Physics, Renmin University, Beijing 100872, China.
‡ Present Address: Forschungszentrum Jülich, JCNS, D-52425 Jülich, Germany.

Received: 3 June 2018; Accepted: 27 June 2018; Published: 3 July 2018

Abstract: Comparative exploration of the nanometer-scale atomic structure of $K_xFe_{2-y}Ch_2$ (*Ch* = S, Se) was performed using neutron total scattering-based atomic pair distribution function (PDF) analysis of 5 K powder diffraction data in relation to physical properties. Whereas $K_xFe_{2-y}Se_2$ is a superconductor with a transition temperature of about 32 K, the isostructural sulphide analogue is not, which instead displays a spin glass semiconducting behavior at low temperatures. The PDF analysis explores phase separated and disordered structural models as candidate descriptors of the low temperature data. For both materials, the nanoscale structure is well described by the iron (Fe)-vacancy-disordered $K_2Fe_{5-y}Ch_5$ ($I4/m$) model containing excess Fe. An equally good description of the data is achieved by using a phase separated model comprised of $I4/m$ vacancy-ordered and $I4/mmm$ components. The $I4/mmm$ component appears as a minority phase in the structure of both $K_xFe_{2-y}Se_2$ and $K_xFe_{2-y}S_2$, and with similar contribution, implying that the phase ratio is not a decisive factor influencing the lack of superconductivity in the latter. Comparison of structural parameters of the Fe-vacancy-disordered model indicates that the replacement of selenium (Se) by sulphur (S) results in an appreciable reduction in the Fe-*Ch* interatomic distances and anion heights, while simultaneously increasing the irregularity of $FeCh_4$ tetrahedra, suggesting the more significant influence of these factors. Structural features are also compared to the non-intercalated FeSe and FeS parent phases, providing further information for the discussion about the influence of the lattice degrees of freedom on the observed properties in layered iron chalcogenides.

Keywords: neutron pair distribution function (PDF); intercalated iron superconductors; anion height; tetrahedron regularity

1. Introduction

Binary $Fe_{1+y}Se$ [1] has attracted considerable attention [2] due to its critical superconducting transition temperature (T_C) up to 8 K at ambient pressure. Externally applied pressure increases the T_C to 37 K at 7 GPa [3], whereas single FeSe layers grown on $SrTiO_3$ show strikingly higher T_Cs (ca. 65 K) [4,5] than many other Fe-based superconductors. Their crystal structure is quasi two-dimensional, composed of slabs of FeSe edge-sharing tetrahedra held together by van der Waals

interactions. Isovalent substitution with sulphur or tellurium for selenium does not change the carrier density [6,7], but substantially modifies the regularity of FeCh_4 (Ch = Se, S, Te) tetrahedron, which is believed to be a crucial factor governing electronic and magnetic properties, having particular influence on electron pairing. Consequently, the chemistry and physics of these simple iron-based materials result in complex relationships in the $Fe_{1+y}Te_{1-x}Se_x$ series [8].

The transition between itinerant antiferromagnetism and superconductivity can be controlled at elevated pressures, but also at ambient pressure by altering the crystal structure through substitutions either at the iron or chalcogen sites and favorably by intercalation of electron donating spacers (guests) between the FeCh sheets. Typically, alkali metals inserted between the FeCh layers expand the lattice and result in a ternary family of iron-superconductors, $A_xFe_2Se_2$ (A = K, Rb, Cs or Tl), with T_Cs in the order of 30 K. The first example of these so-called 122-iron selenides, the $K_{0.8}Fe_2Se_2$ derivative [9,10], was shown to adopt a $ThCr_2Si_2$-type structure. Much like the iron-pnicitides, with Fe tetrahedrally coordinated, superconductivity remains at the boundary with antiferromagnetism. However, whereas pnictides display superconductivity in the fully occupied, stoichiometric $ThCr_2Si_2$ structure, divalent Se^{2-} (instead of trivalent As^{3-}) leads to the presence of alkali and iron vacancies and issues of chemical instability that is promoted by the high-temperature solid-state synthesis of the $K_xFe_{2-y}Se_2$ compounds. This entails microscale phase separation, with heterogeneity creating less than 20% of $I4/mmm$ $K_xFe_2Se_2$, adopting the iron-pnictide $ThCr_2Si_2$ superconducting crystal structure, and the majority $I4/m$ $K_2Fe_4Se_5$ Fe-vacancy-ordered antiferromagnetic phase (Figure 1) [11,12]. The origin of superconductivity and the precise stoichiometry of iron and potassium content that leads to the superconducting phase are still under debate owing to the intrinsic phase separation and inhomogeneity in this type of chemically complex material [13,14]. Interestingly, the substitution of Se for S in the $K_xFe_{2-y}Se_{2-z}S_z$ ($0 \leq z \leq 2$) series suppresses the superconducting state (z = 1.6) [15] and eventually the sulphide end-member, $K_xFe_{2-y}S_2$, is not superconducting but exhibits a spin-glass behavior at temperatures below 32 K [16]. Therefore, experimental efforts to understand superconductivity in iron chalcogenides must not only tackle the sensitive stoichiometry required to observe a sizeable T_C, but also decipher the subtle differences in the atomic structure configuration that lead to such markedly different physical properties.

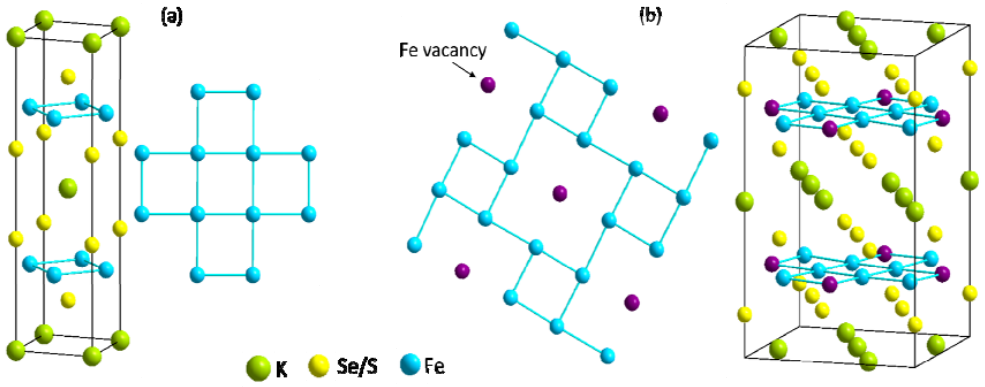

Figure 1. Atomic structure models for KFe_2Ch_2: (**a**) $I4/mmm$ featuring fully occupied Fe-layers and (**b**) $I4/m$, exhibiting Fe-vacancy order. Combinations of these models (not shown) were also used in the study.

Here, we use neutron total scattering experiments combined with atomic pair distribution function (PDF) analysis [17] to explore the nanometer scale aspects of phase separation and inhomogeneity for the two end-members of $K_xFe_{2-y}Se_{2-z}S_z$ (z = 0, 2) series, at 5 K. We probe their structural evolution based on the regularity of the FeCh_4 tetrahedra and the Fe anion heights, which have been considered before as empirical parameters that mediate the evolution of the superconducting critical temperature in these intercalated materials.

2. Materials and Methods

Powdered samples of $K_xFe_{2-y}Se_2$ and $K_xFe_{2-y}S_2$ were prepared by pulverizing single crystals stored in a glove box. The single crystals were synthesized and characterized according to protocols reported previously [15]. Laboratory X-ray powder diffraction data of the samples used in this study were fully indexed within the *I*4/*m* space group. Low temperature magnetic susceptibility and electrical resistivity measurements of the materials were previously reported [15]. The selenium-containing sample exhibited bulk superconductivity at T_C = 33 K, whereas the sulfur-containing sample was not superconducting and displayed magnetic semi-metallic behavior at low temperatures.

The neutron total scattering experiment was performed at the Nanoscale-Ordered Materials Diffractometer (NOMAD) [18] at the Spallation Neutron Source at Oak Ridge National Laboratory. Two pulverized samples, approximately 0.5 g each, were sealed in helium atmosphere in extruded cylindrical vanadium containers 6 mm in diameter, and mounted in the diffractometer equipped with an Orange cryostat sample environment. The instrument was calibrated using diamond standard. The data for each sample were collected at 5 K for 60 min. Data reduction was performed following standard protocols described elsewhere [19]. Pair distribution functions were obtained by Sine Fourier transformation of the measured reduced total scattering functions F(Q), where Q is the momentum transfer, over a range of Q_{MIN} = 0.5 Å^{-1} to Q_{MAX} = 26 Å^{-1}. Refinement of the structural models against the experimental PDF data was completed over a 1 nm range via the small-box approach used within the PDFGUI software suite [20].

3. Results and Discussion

3.1. Qualitative Data Comparison

We began by observing and comparing the raw neutron powder diffraction data for $K_xFe_{2-y}Se_2$ and $K_xFe_{2-y}S_2$ shown in Figure 2, as seen by the forward scattering bank of detectors. Notably, this detector bank provided rather poor resolution featuring broad peaks and inherently lower statistics. This is a consequence of the construction of the NOMAD instrument, which is optimized for total scattering type measurements, where broad Q-range coverage and high resolution in backscattering banks are far more important, at the expense of the low angle banks. Nevertheless, for both, the data clearly identify the presence of, albeit weak, intensity associated with the (110) reflection that is a hallmark of *I*4/*m* and is absent in *I*4/*mmm* symmetry. This qualitative assessment revealed that both systems have, at least in part, *I*4/*m* structural character, in agreement with previous reports [15,16].

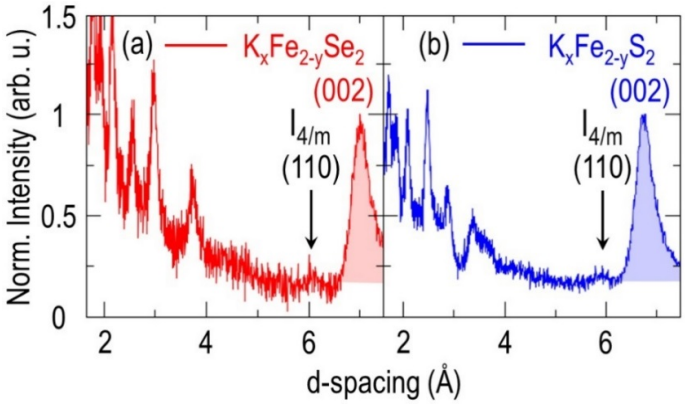

Figure 2. Neutron powder diffraction intensities for forward scattering 2θ = 15° NOMAD detector bank over selected d-spacing range. For easier comparison, the patterns were normalized to the intensities of (002) reflections (shaded): (**a**) $K_xFe_{2-y}Se_2$ and (**b**) $K_xFe_{2-y}S_2$. Arrows mark the (110) reflection that is allowed in the *I*4/*m* but not in the *I*4/*mmm* symmetry.

The neutron total scattering data collected over a broad range of momentum transfer Q were examined next. The findings are illustrated in Figure 3a,b for $K_xFe_{2-y}Se_2$ and $K_xFe_{2-y}S_2$, respectively, in the form of reduced total scattering structure function F(Q). Observable are appreciable arcs of diffuse scattering, particularly at higher momentum transfer values, indicative of appreciable disorder, as expected for this class of materials. Fourier transforms of F(Q) resulted in PDF and G(r), that are presented in Figure 3c,d, respectively. Some of the PDF peaks appear more intense in the $K_xFe_{2-y}Se_2$ pattern than in that of $K_xFe_{2-y}S_2$. In principle, this could be due to the differences in the underlying bond-length distributions reflecting the nanoscale structures and the complexity of underlying disorder. However, the coherent neutron scattering lengths, which scale the individual PDF contributions of any given pair of atoms in the structure, are nearly three times larger for selenium than for sulfur (b(Se) = 7.970 fm, whereas b(S) = 2.847 fm). The change in relative PDF peak intensity also originates from the renormalization due to different scattering properties of the samples.

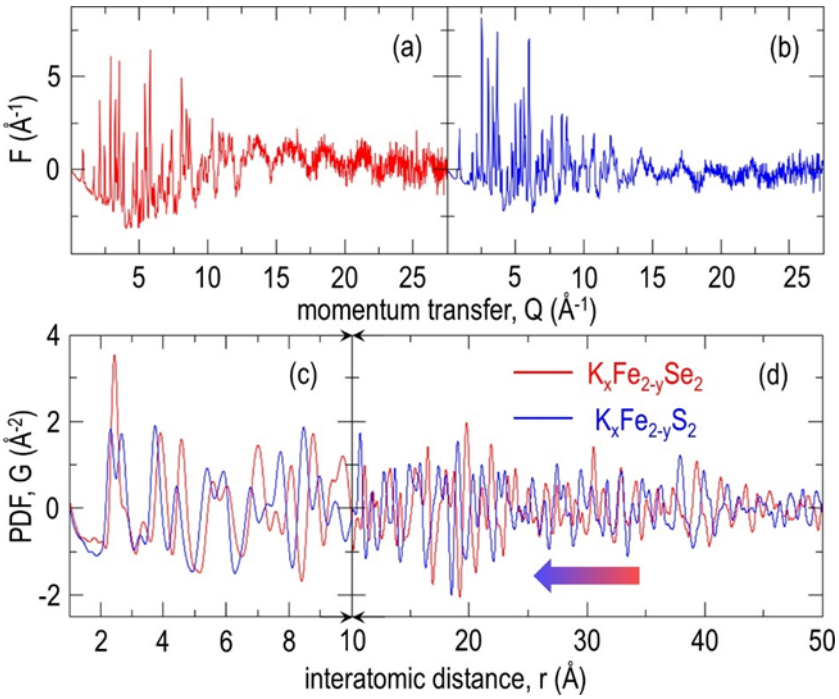

Figure 3. Neutron total scattering data for $K_xFe_{2-y}Ch_2$ (*Ch* = S, Se) at 5 K. Reduced neutron total scattering structure function, F(Q), for (**a**) $K_xFe_{2-y}Se_2$ (red) and (**b**) $K_xFe_{2-y}S_2$ (blue). Corresponding PDF data for $K_xFe_{2-y}Se_2$ (red) and $K_xFe_{2-y}S_2$ (blue) over a 5-nm PDF field of view are displayed below. (**c**) The low-r region is shown on an expanded scale, as compared to (**d**), which features intermediate distance range. The block arrow indicates the volume reduction trend from *Ch* = Se to S.

The PDFs of the two samples studied were directly compared in Figure 3. Notably, the PDF pattern of the sulphide is shifted considerably to lower interatomic distances, *r*, as indicated by the block arrow in Figure 3d, compared to the selenide counterpart. This lattice contraction occurred due to the lower ionic size of S^{2-} (ionic radius 1.84 Å) compared to that of Se^{2-} (ionic radius 1.98 Å) [21]. By examining the very local scale (Figure 3c), observably narrower bond-length distribution pertaining to the FeCh_4 tetrahedral environments was apparent in $K_xFe_{2-y}Se_2$ compared with $K_xFe_{2-y}S_2$. However, considering the appreciably different neutron scattering lengths of Se and S, as well as their effective radii, this assertion requires further confirmation from explicit structural modeling.

3.2. Model Dependent PDF Analysis

Structural information from experimental PDFs was extracted using the small box modeling approach based on small symmetrized unit cells (typically ~10 to 100 atoms) [17]. This approach provides a simple framework for crystal structure interpretation at the expense of being limited to the symmetry constraints of the underlying models. The approach was previously reported in detail [20].

Our modeling was based on the two phases described above and shown in Figure 1. The phase with *I*4/*mmm* symmetry, often referred to as metallic, features stoichiometric slabs of FeCh_4 tetrahedra, whereas the phase with *I*4/*m* symmetry, considered insulating and antiferromagnetic, contains two symmetrically distinct Fe crystallographic sites, one of which features Fe-vacancies and is completely empty in the case of full vacancy order. Here, we refer to the latter as the Fe-vacancy-ordered (*I*4/*m* VO) model. In this model, the Fe and K occupancies at the low multiplicity sites, *4d* and *2b*, respectively, were fixed to zero under the assumption that all Fe and K atoms reside only at the high multiplicity sites, *16i* and *8h*, consistent with our room temperature Rietveld refinements reported earlier [22]. In addition, we considered a modified version of the *I*4/*m* model, in which the occupancy of the Fe-vacancy *4d* site was allowed to vary, which we refer to as the vacancy-disordered (*I*4/*m* VD) model. We used these atomic configurations both individually in single phase fits and combined in two-phase refinements. All fractional coordinates were constrained to follow the respective space group symmetries. All atomic displacement parameters (ADP) were set to be isotropic and identical for all atomic species of the same type. The occupancy and ADP constraints were introduced to minimize the number of refined parameters and to enable the sensible semiquantitative comparison of the two systems within the realm of these models. Although various model combinations were tested, the two that showed the best agreement with the data were (1) two-phase mixture composed of *I*4/*mmm* and *I*4/*m* VO ingredient phases, and (2) single phase *I*4/*m* VD model. We limit our discussion to these two models.

The refinements of the structural models that result in the lowest fit residual (R_W) are summarized in Figure 4a for selenide and in Figure 4b for sulphide. The refinements results revealed that, at the nanoscale, the structures of both $K_xFe_{2-y}Se_2$ and $K_xFe_{2-y}S_2$ within the sensitivity of our data, were consistent with both a two-phase mixture (metallic *I*4/*mmm* and insulating *I*4/*m* VO) model and with a single phase disordered *I*4/*m* VD model. Previous reports confirmed the coexistence of these two phases in both selenide [22] and sulphide analogue [23]. Notably, the single phase *I*4/*m* VD model is effectively equivalent to a phase separated model, albeit disordered. In the explicit two-phase modeling of the selenide and sulphide data, the majority phase was found to be the *I*4/*m* VO with a percentage of ca. 89(5)% and ca. 73(8)% by weight, respectively. Notably, according to this step in the analysis, the minority phase *I*4/*mmm* in the case of $K_xFe_{2-y}S_2$ exhibited a higher percentage in the phase mixture than $K_xFe_{2-y}Se_2$. Whereas the exact phase percentage is difficult to acquire and is somewhat dependent on the type of constraints used, the robust observation in all our fits was that the metallic *I*4/*mmm* phase contribution in non-superconducting $K_xFe_{2-y}S_2$ was at least comparable or probably slightly larger than in superconducting $K_xFe_{2-y}Se_2$. This implied that the presence or absence of this phase is not the sole factor that affects the superconductivity in this system. Furthermore, the phase separation picture on the nanoscale likely represents an oversimplification of the true complexity of the system, and may possibly reflect the limitations of the small box modeling approach.

We next explored the vacancy-disordered $K_2Fe_{5-y}Ch_5$ *I*4/*m* VD model in which the Fe occupancy at the *4d* site is explicitly refined. The Fe occupancy at the high multiplicity *16i* site was fixed to one, as an attempt to explicitly refine the marginal deviations, in agreement with previous reports. Although attempts to refine K-content were made, this resulted in fit instabilities and the correlation of refined parameters was indicative of over-parametrization, so the occupancy of K sites was adjusted in all models to reflect nominal 0.8 potassium content. In *I*4/*m*-type models, the K *2b* site was empty. Importantly, the refinement results were qualitatively very similar to those of the phase mixture model. The refinements show finite and similar Fe occupancies at the *4d* site in both materials, which increase the overall Fe content to $K_2Fe_{4.27(1)}Se_5$ and $K_2Fe_{4.27(1)}S_5$, indicating no substantial difference across

the two systems in terms of phase-separation sensitive parameters and within the limitations of the applied modeling methodology. We interpreted this as an indicator that the phase separation aspect is not of fundamental importance for the lack of superconductivity in the sulphide, in the sense that non-superconducting sulphide does not account for a smaller fraction of the metallic phase.

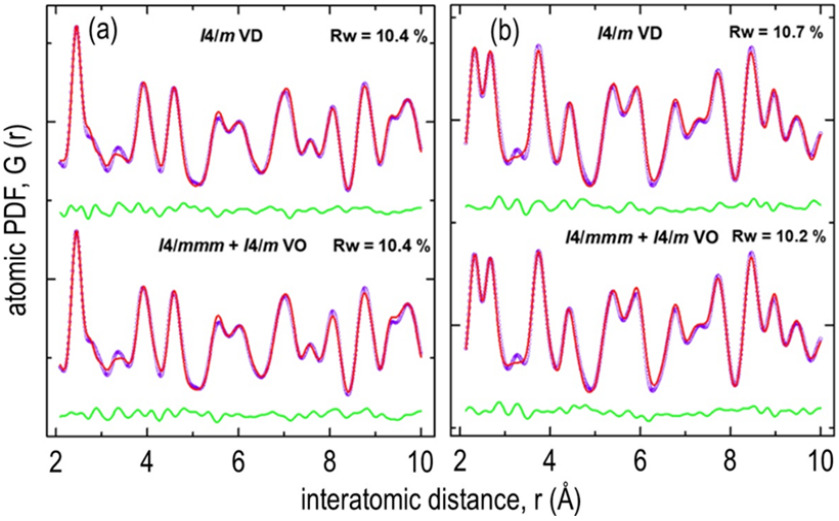

Figure 4. Refinements of neutron total scattering PDF data of (**a**) $K_xFe_{2-y}Se_2$ and (**b**) $K_xFe_{2-y}S_2$ at 5 K for the two structural models discussed in the text: (1) two-phase mixture of *I*4/*mmm* KFe_2Ch_2 and *I*4/*m* VO $K_2Fe_4Ch_5$ (bottom row), and (2) single phase *I*4/*m* VD $K_2Fe_{5-y}Ch_5$ (top row). Observed (blue open symbols), calculated (red solid line), and difference (green solid line, offset for clarity) PDF profiles are illustrated. Fit residuals R_W are also shown.

In Tables 1 and 2, we quantitatively compare various structural parameters derived from the single-phase *I*4/*m* VD model at 5 K, such as lattice parameters, interatomic Fe-*Ch* and Fe-Fe distances, anion heights, and ADP values. Most values are compared in reference to respective quantities obtained for non-intercalated FeSe [24] and FeS [25] parent materials. As expected, the lattice parameters and the interatomic distances (all Fe-*Ch* and the inter-cluster Fe-Fe lengths) are longer in the case of selenide, resulting in a large increase in the unit cell volume of ca. 11%. In the K-intercalated systems, two types of Fe-Fe distances are associated with the square Fe clusters: intracluster and intercluster, as defined within the *I*4/*m* model. In the FeSe reference, there are two distinct Fe-Fe distances; however, these are along the two distinct crystallographic directions, as defined by the orthorhombic *Cmma* model.

Table 1. Lattice parameters, interatomic Fe-*Ch* distances (d) and anion heights obtained from PDF refinements of *I*4/*m* VD model to the $K_2Fe_{5-y}Ch_5$ 5 K data (*Ch* = Se, S). Neutron powder diffraction results for FeSe at 10 K [24] and x-ray powder diffraction results for FeS at 300 K [25] are also shown as a reference.

I*4/*m	**a = b (Å)**	**c (Å)**	**d_1 (Å) [1]**	**d_2 (Å) [2]**	**d_3 (Å) [2]**	**d_4 (Å) [2]**	**h_{Ch} (Å)**
$K_2Fe_{4.27(1)}Se_5$	8.683(1)	14.001(3)	2.337(8)	2.446(2)	2.451(3)	2.512(5)	1.396(9)
$K_2Fe_{4.27(1)}S_5$	8.395(2)	13.437(2)	2.283(5)	2.321(8)	2.332(5)	2.37(1)	1.282(8)
Cmma	**a (Å)**	**b (Å)**	**c (Å)**	**d (Å) × 4**	-	-	**h_{Ch} (Å)**
FeSe	5.3147(5)	5.3367(5)	5.4855(3)	2.383(1)	-	-	1.461(2)
P*4/*nmm	**a = b (Å)**	**c (Å)**	**d (Å) × 4**	-	-	-	**h_{Ch} (Å)**
FeS	3.6802(5)	5.0307(7)	2.235(1)	-	-	-	1.270(1)

[1] Fe-*Ch*(1) distance, where *Ch*(1) belongs to *4e* site; [2] Fe-*Ch*(2) distances, where *Ch*(2) belongs to *16i* site.

Table 2. Interatomic Fe-Fe distances and isotropic ADPs from the PDF refinements of *I*4/*m* VD model to the $K_2Fe_{5-y}Ch_5$ data (*Ch* = Se, S) at 5 K and neutron powder diffraction refinement for FeSe at 10 K.

I*4/*m	**Intra-Cluster Fe-Fe (Å)**	**Inter-Cluster Fe-Fe (Å)**	**K, Uiso (Å^2)**	**Fe, Uiso (Å^2)**	***Ch*, Uiso (Å^2)**
$K_2Fe_{4.27(1)}Se_5$	2.649(4)	2.897(5)	0.0231(7)	0.0087(1)	0.0067(1)
$K_2Fe_{4.27(1)}S_5$	2.672(1)	2.746(1)	0.0236(2)	0.0093(1)	0.0032(1)
Cmma	**Fe-Fe(1) (Å)**	**Fe-Fe(2) (Å)**			
FeSe	2.657(1)	2.667(1)	-	0.0043(7)	0.0033(9)

One prominent structural parameter known to be correlated with the superconducting transition temperature T_C in iron-based superconductors is the anion height, defined as the *c*-axis normal distance between the chalcogen/pnictogen and the Fe-sheet. According to this empirical observation, the critical temperature, T_C increases as the anion height approaches a value of ~1.38 Å, inferring the existence of an optimal bonding environment for maximizing the superconducting response [26]. The anion height values obtained for the samples studied here were generally consistent with the empirical rule established by Mizuguchi et al. [26]. For our superconducting $K_2Fe_{4.27(1)}Se_5$ sample, with $T_C \approx 32$ K, the anion height was indeed relatively close to this ideal value, whereas for the insulating $K_2Fe_{4.27(1)}S_5$ material, the anion height was appreciably further away from the optimal 1.38 Å. This is illustrated schematically in the inset of Figure 5. The replacement of Se by smaller S results in reduction of all interatomic cation-anion distances, which in turn gives rise to a decrease in the anion height to about ~1.28 Å. The anion height in the potassium-intercalated selenide can also be compared to the parent FeSe, which crystallizes in the *Cmma* structure at low temperatures. For the latter, the neutron powder diffraction data collected at 10 K on the same instrument were used [24]. Intercalation of K in between the FeSe layers induced an effective reduction in the anion height, shifting the value closer to the optimum, while simultaneously increasing the Fe-interlayer spacing from 5.316(1) Å to 7.001(1) Å, with a concomitant increase of T_C from about 8 K to about 32 K. In the sulphide analogue, the K intercalation also increased the Fe interlayer spacing from 5.031(1) Å to 6.747(4) Å, but the anion height increased only slightly, and at 1.28 Å, is still substantially far from the optimum value for superconductivity. Whereas FeS is a superconductor with a T_C ~5 K [25], the K-intercalated compound exhibited a spin-glass behavior.

Lastly, we considered the regularity of the FeCh_4 tetrahedron, which represents yet another structural aspect of relevance to superconductivity [12,15,27]. Indeed, the superconducting critical temperature T_C in some iron-based superconductors was maximized for structures featuring regular tetrahedral units, defined by the *Ch*-Fe-*Ch* angles all being equal to 109.47°, thus resulting in perfect tetrahedral geometry. Given this, the mean and standard deviation of the underlying bond angle distributions were estimated from the neutron scattering data analyzed for the systems of interest here. To facilitate the comparison, the data are schematically presented as Gaussian distributions in Figure 5, whose centroids reflect the average tetrahedral angle, whereas the widths represent the standard deviation of the angular distribution. For the samples studied, these values were obtained for the six tetrahedral angles of $K_2Fe_{5-y}Ch_5$ (*Ch* = Se, S) based on the *I*4/*m* VD model for *16i* Fe site, and the three angles of FeSe (with multiplicity two) assuming an orthorhombic *Cmma* crystal type. In the case of FeS, the distribution was the narrowest (not shown), implying that the tetrahedral regularity is not a required condition for optimizing superconductivity. Nevertheless, PDF results evidenced a larger degree of tetrahedral irregularity in the case of $K_2Fe_{5-y}S_5$ as compared with $K_2Fe_{5-y}Se_5$. Replacement of Se by S substantially increased the irregularity of the FeCh_4 tetrahedron on average, which, together with the substantial departure of the anion height from the optimum value, coincide with the observed decrease in superconductivity and the appearance of the spin glass state in the sulphide. These modeling results confirm the narrower distribution of interatomic distances in the selenide, determined from the direct comparison of the experimental PDFs. Importantly,

the parent FeSe showed a slightly wider distribution compared with the K-intercalated counterpart, and consistently lower value of T_C. As the anion heights of the selenide and sulfide samples studied here were positioned on the opposite sides of the optimal value of 1.38 Å, where the observed T_C peaks in iron chalcogenides and pnictides, tracking this subtle structural parameter on the basis of the $K_xFe_{2-y}Se_{2-z}S_z$ solid-solution testing ground would be valuable. In particular, systematically and quantitatively characterizing the evolution of the disorder across the phase diagram of $K_xFe_{2-y}Se_{2-z}S_z$ at low temperatures would help correlate how the key building blocks relay the competition of magnetism with superconductivity (and vice versa), a concept of fundamental importance in Fe-based correlated electron systems.

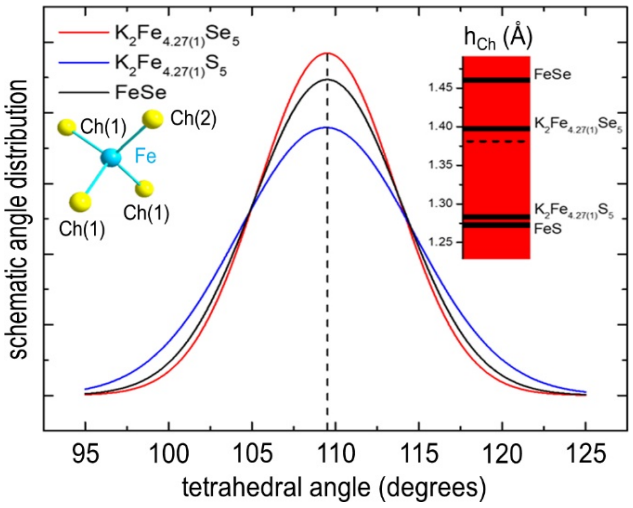

Figure 5. Schematic of the tetrahedral angle distribution (solid lines) extracted from the tetrahedral angles of the Fe *16i* site in $K_2Fe_{5-y}Ch_5$ *I*4/*m* VD PDF model at 5 K and for FeSe in the *Cmma* symmetry at 10 K. The vertical dashed line marks the ideal tetrahedral angle of 109.47°. The inset (red bar) illustrates the placement of the average anion height h_{Ch} (black lines) for the material systems considered relative to the optimal value of ~1.38 Å (dashed line).

4. Conclusions

In summary, we performed a neutron PDF analysis to explore the nanoscale atomic structures of two $K_xFe_{2-y}Ch_2$ materials (*Ch* = S, Se) at 5 K. The study was motivated by the phase separation concept in these compositions, which enabled the comparison of their structural features to those observed in their non-intercalated counterparts. Interestingly, the diffraction patterns of both systems displayed the (110) reflection, a hallmark of *I*4/*m* crystal symmetry. In the respective reduced total scattering structure functions F(Q), appreciable arcs of diffuse scattering, particularly at high momentum transfers Q, were indicative of the presence of substantial disorder in the system. The diffuse intensity appeared to be more pronounced for $K_xFe_{2-y}Se_2$ than for $K_xFe_{2-y}S_2$. The PDF analysis revealed that the data for both systems could be explained by either a mixture of majority *I*4/*m* vacancy-ordered and minority *I*4/*mmm* components, or by a single phase *I*4/*m* vacancy-disordered model. Both descriptions are effectively consistent with the underlying phase separation and complex disorder on the nanoscale. Quantitatively, in the two-phase description, the *I*4/*mmm* minority phase content did not decrease from $K_xFe_{2-y}Se_2$ to $K_xFe_{2-y}S_2$ as would be expected on the grounds that this phase is commonly associated with superconductivity. Similarly, the single-phase vacancy disordered model description resulted in comparable values of the occupancy of the Fe *4d* site for the two systems. This indicates that the potassium intercalated Fe*Ch* is more complex than outlined by the simplistic phase separation scenario, and implies that the phase separation does not play a key role in the collapse of superconductivity in the intercalated sulphide system. An explanation might be provided by the fine details of

disorder that are yet to be explored. Comparison of relevant structural parameters derived from the Fe-vacancy-disordered model demonstrated that replacement of larger Se by smaller S induced a dramatic reduction in the unit cell volume and interatomic Fe-*Ch* distances. Corresponding anion heights conformed to the empirical rule of Mizuguchi et al. [26]. Furthermore, the FeCh_4 tetrahedra were more irregular in the non-superconducting sulphide than in the superconducting selenide. The same parameters obtained for the non-intercalated parent materials appear to also follow the same empirical trend. Overall, this neutron total scattering study highlights that deciphering the subtle differences in the atomic structure configuration of the K-intercalated end-members and their markedly different physical properties is a complex physical crystallography problem. Seeking additional insights from $K_xFe_{2-y}Se_{2-z}S_z$ solid-solutions may be crucial for uncovering the mediating role of key structural building blocks in this puzzle.

Author Contributions: Project conceived by E.S.B., A.L. and C.P.; Sample preparation and characterization, H.L. and C.P.; Data acquisition, E.S.B. and M.F.; Data reduction, M.F., E.S.B. and M.T.M.; Data modeling and interpretation, P.M., A.L. and E.S.B.; Writing-Original Draft Preparation, P.M., A.L. and E.S.B.; Writing-Review, all co-authors; Writing-Final Editing, P.M., C.P., A.L. and E.S.B.

Funding: This research used resources at the Spallation Neutron Source, a U.S. Department of Energy Office of Science User Facility operated by the Oak Ridge National Laboratory. Alexandros Lappas acknowledges support by the U.S. Office of Naval Research Global, NICOP grant award No. N62909-17-1-2126. Work at Brookhaven National Laboratory was supported by U.S. Department of Energy, Office of Science, Office of Basic Energy Sciences (DOE-BES) under contract DE-SC0012704 and by the Center for Emergent Superconductivity, an Energy Frontier Research Center funded by the U.S. Department of Energy, Office for Basic Energy Science (Hechang Lei and Cedomir Petrovic).

Conflicts of Interest: The authors declare no conflict of interest.

References

1. Hsu, F.-C.; Luo, J.-Y.; Yeh, K.-W.; Chen, T.-K.; Huang, T.-W.; Wu, P.M.; Lee, Y.-C.; Huang, Y.-L.; Chu, Y.-Y.; Yan, D.-C.; et al. Superconductivity in the PbO-type structure α-FeSe. *Proc. Natl. Acad. Sci. USA* **2008**, *105*, 14262–14264. [CrossRef] [PubMed]
2. Malavasi, L.; Margadonna, S. Structure–properties correlations in Fe chalcogenide superconductors. *Chem. Soc. Rev.* **2012**, *41*, 3897–3911. [CrossRef] [PubMed]
3. Margadonna, S.; Takabayashi, Y.; Ohishi, Y.; Mizuguchi, Y.; Takano, Y.; Kagayama, T.; Nakagawa, T.; Takata, M.; Prassides, K. Pressure evolution of the low-temperature crystal structure and bonding of the superconductor FeSe (T_C = 37 K). *Phys. Rev. B* **2009**, *80*, 064506. [CrossRef]
4. Tan, S.; Zhang, Y.; Xia, M.; Ye, Z.; Chen, F.; Xie, X.; Peng, R.; Xu, D.; Fan, Q.; Xu, H.; et al. Interface-induced superconductivity and strain-dependent spin density waves in FeSe/$SrTiO_3$ thin films. *Nat. Mater.* **2013**, *12*, 634–640. [CrossRef] [PubMed]
5. Ge, J.-F.; Liu, Z.-L.; Liu, C.; Gao, C.-L.; Qian, D.; Xue, Q.-K.; Liu, Y.; Jia, J.-F. Superconductivity above 100 K in single-layer FeSe films on doped $SrTiO_3$. *Nat. Mater.* **2015**, *14*, 285–289. [CrossRef] [PubMed]
6. Fang, M.H.; Pham, H.M.; Qian, B.; Liu, T.J.; Vehstedt, E.K.; Liu, Y.; Spinu, L.; Mao, Z.Q. Superconductivity close to magnetic instability in $Fe(Se_{1-x}Te_x)_{0.82}$. *Phys. Rev. B* **2008**, *78*. [CrossRef]
7. Yeh, K.-W.; Huang, T.-W.; Huang, Y.; Chen, T.-K.; Hsu, F.-C.; Wu, P.M.; Lee, Y.-C.; Chu, Y.-Y.; Chen, C.-L.; Luo, J.-Y.; et al. Tellurium substitution effect on superconductivity of the α-phase iron selenide. *EPL Europhys. Lett.* **2008**, *84*, 37002. [CrossRef]
8. Katayama, N.; Ji, S.; Louca, D.; Lee, S.; Fujita, M.; Sato, T.J.; Wen, J.; Xu, Z.; Gu, G.; Xu, G.; et al. Investigation of the Spin-Glass Regime between the Antiferromagnetic and Superconducting Phases in $Fe_{1+y}Se_xTe_{1-x}$. *J. Phys. Soc. Jpn.* **2010**, *79*, 113702. [CrossRef]
9. Guo, J.; Jin, S.; Wang, G.; Wang, S.; Zhu, K.; Zhou, T.; He, M.; Chen, X. Superconductivity in the iron selenide $K_xFe_2Se_2$ ($0 \leq x \leq 1.0$). *Phys. Rev. B* **2010**, *82*. [CrossRef]
10. Ye, F.; Chi, S.; Bao, W.; Wang, X.F.; Ying, J.J.; Chen, X.H.; Wang, H.D.; Dong, C.H.; Fang, M. Common Crystalline and Magnetic Structure of Superconducting $A_2Fe_4Se_5$ (A = K, Rb, Cs, Tl) Single Crystals Measured Using Neutron Diffraction. *Phys. Rev. Lett.* **2011**, *107*, 137003. [CrossRef] [PubMed]

11. Shoemaker, D.P.; Chung, D.Y.; Claus, H.; Francisco, M.C.; Avci, S.; Llobet, A.; Kanatzidis, M.G. Phase relations in $K_xFe_{2-y}Se_2$ and the structure of superconducting $K_xFe_2Se_2$ via high-resolution synchrotron diffraction. *Phys. Rev. B* **2012**, *86*. [CrossRef]
12. Vivanco, H.K.; Rodriguez, E.E. The intercalation chemistry of layered iron chalcogenide superconductors. *J. Solid State Chem.* **2016**, *242*, 3–21. [CrossRef]
13. Carr, S.V.; Louca, D.; Siewenie, J.; Huang, Q.; Wang, A.; Chen, X.; Dai, P. Structure and composition of the superconducting phase in alkali iron selenide $K_yFe_{1.6+x}Se_2$. *Phys. Rev. B* **2014**, *89*, 134509. [CrossRef]
14. Tanaka, M.; Yanagisawa, Y.; Denholme, S.J.; Fujioka, M.; Funahashi, S.; Matsushita, Y.; Ishizawa, N.; Yamaguchi, T.; Takeya, H.; Takano, Y. Origin of the Higher-T_c Phase in the $K_xFe_{2-y}Se_2$ System. *J. Phys. Soc. Jpn.* **2016**, *85*, 044710. [CrossRef]
15. Lei, H.; Abeykoon, M.; Bozin, E.S.; Wang, K.; Warren, J.B.; Petrovic, C. Phase Diagram of $K_xFe_{2-y}Se_{2-z}S_z$ and the Suppression of its Superconducting State by an Fe2-Se/S Tetrahedron Distortion. *Phys. Rev. Lett.* **2011**, *107*. [CrossRef] [PubMed]
16. Lei, H.; Abeykoon, M.; Bozin, E.S.; Petrovic, C. Spin-glass behavior of semiconducting $K_xFe_{2-y}S_2$. *Phys. Rev. B* **2011**, *83*. [CrossRef]
17. Billinge, S.J.L.; Egami, T. *Underneath the Bragg Peaks: Structural Analysis of Complex Materials*; Pergamon Materials Series; Elsevier: Oxford, UK, 2003; Volume 7.
18. Neuefeind, J.; Feygenson, M.; Carruth, J.; Hoffmann, R.; Chipley, K.K. The Nanoscale Ordered MAterials Diffractometer NOMAD at the Spallation Neutron Source SNS. *Nucl. Instrum. Methods Phys. Res. Sect. B* **2012**, *287*, 68–75. [CrossRef]
19. Peterson, P.F.; Gutmann, M.; Proffen, T.; Billinge, S.J.L. PDFgetN: A user-friendly program to extract the total scattering structure factor and the pair distribution function from neutron powder diffraction data. *J. Appl. Crystallogr.* **2000**, *33*, 1192. [CrossRef]
20. Farrow, C.L.; Juhas, P.; Liu, J.W.; Bryndin, D.; Božin, E.S.; Bloch, J.; Proffen, T.; Billinge, S.J.L. PDFfit2 and PDFgui: Computer programs for studying nanostructure in crystals. *J. Phys. Condens. Matter* **2007**, *19*, 335219. [CrossRef] [PubMed]
21. Shannon, R.D. Revised effective ionic radii and systematic studies of interatomic distances in halides and chalcogenides. *Acta Crystallogr. Sect. A* **1976**, *32*, 751–767. [CrossRef]
22. Lazarević, N.; Abeykoon, M.; Stephens, P.W.; Lei, H.; Bozin, E.S.; Petrovic, C.; Popović, Z.V. Vacancy-induced nanoscale phase separation in $K_xFe_{2-y}Se_2$ single crystals evidenced by Raman scattering and powder X-ray diffraction. *Phys. Rev. B* **2012**, *86*. [CrossRef]
23. Tsuchiya, Y.; Ikeda, S.; Zhang, X.-W.; Kishimoto, S.; Kikegawa, T.; Hirao, N.; Kawaguchi, S.I.; Ohishi, Y.; Kobayash, H. Pressure-Induced Phase Transition in $K_xFe_{2-y}S_2$. *J. Phys. Soc. Jpn.* **2017**, *86*. [CrossRef]
24. Xu, Z.; Schneeloch, J.A.; Wen, J.; Božin, E.S.; Granroth, G.E.; Winn, B.L.; Feygenson, M.; Birgeneau, R.J.; Gu, G.; Zaliznyak, I.A.; et al. Thermal evolution of antiferromagnetic correlations and tetrahedral bond angles in superconducting $FeTe_{1-x}Se_x$. *Phys. Rev. B* **2016**, *93*, 104517. [CrossRef]
25. Lai, X.; Zhang, H.; Wang, Y.; Wang, X.; Zhang, X.; Lin, J.; Huang, F. Observation of Superconductivity in Tetragonal FeS. *J. Am. Chem. Soc.* **2015**, *137*, 10148–10151. [CrossRef] [PubMed]
26. Mizuguchi, Y.; Hara, Y.; Deguchi, K.; Tsuda, S.; Yamaguchi, T.; Takeda, K.; Kotegawa, H.; Tou, H.; Takano, Y. Anion height dependence of T_c for the Fe-based superconductor. *Supercond. Sci. Technol.* **2010**, *23*, 054013. [CrossRef]
27. Lee, C.-H.; Iyo, A.; Eisaki, H.; Kito, H.; Fernandez-Diaz, M.T.; Ito, T.; Kihou, K.; Matsuhata, H.; Braden, M.; Yamada, K. Effect of Structural Parameters on Superconductivity in Fluorine-Free $LnFeAsO_{1-y}$ (Ln = La, Nd). *J. Phys. Soc. Jpn.* **2008**, *77*, 083704. [CrossRef]